POLITECNICO DI TORINO
Repository ISTITUZIONALE

Physicochemical properties and redox behaviour of Fe-doped hybrid nanotubes of the imogolite type and their rGO nanocomposites

Original
Physicochemical properties and redox behaviour of Fe-doped hybrid nanotubes of the imogolite type and their rGO nanocomposites / Serrapede, M., Rivolo, P., Manzoli, M., Armandi, M., Fontana, M., Arcoraci, D., Pirri, C.F., Esposito, S., Bonelli, B.. - In: APPLIED CLAY SCIENCE. - ISSN 0169-1317. - 247:(2024). [10.1016/j.clay.2023.107202]

Availability:
This version is available at: 11583/2983645 since: 2023-11-13T10:33:59Z

Publisher:
Elsevier

Published
DOI:10.1016/j.clay.2023.107202

Terms of use:

This article is made available under terms and conditions as specified in the corresponding bibliographic description in the repository

Publisher copyright
Elsevier postprint/Author's Accepted Manuscript

© 2024. This manuscript version is made available under the CC-BY-NC-ND 4.0 license
http://creativecommons.org/licenses/by-nc-nd/4.0/.The final authenticated version is available online at:
http://dx.doi.org/10.1016/j.clay.2023.107202

(Article begins on next page)

09 October 2026

"Physicochemical properties and redox behaviour of Fe-doped hybrid nanotubes of the imogolite type and their rGO nanocomposites"

Mara Serrapede,[1,2] Paola Rivolo,[1] Maela Manzoli,[3] Marco Armandi,[1] Marco Fontana,[1] Davide Arcoraci,[1] Candido Fabrizio Pirri,[1,2] Serena Esposito,[1] Barbara Bonelli. [1,4]*

[1]*Department of Applied Science and Technology and INSTM Unit of Torino – Politecnico, Corso Duca degli Abruzzi 24, I-10129, Torino (Italy).*

[2] *Center for Sustainable Future Technologies @POLITO, Istituto Italiano di Tecnologia, Via Livorno 60, Torino, I-10144 (Italy).*

[3]*Department of Drug Science and Technology, Università degli Studi di Torino, Via P. Giuria 9, I-10125 Torino (Italy).*

[4]*Interdepartmental Centre PolitoBIOMed Lab, Corso Duca degli Abruzzi 24, Torino, I-10129 (Italy).*

Corresponding author: barbara.bonelli@polito.it; Tel.: +39-0110904719

Abstract

By ionic exchange of preformed methylimogolite nanotubes (chemical formula $(OH)_3Al_2O_3SiCH_3$), nanotubes with the chemical formula $(OH)_3Al_{2-x}Fe_xO_3SiCH_3$ were obtained, with *x* values of 0.05 and 0.1, corresponding to a nominal Fe content of 1.4 and 2.8 wt.%, respectively. The nanotubes were characterized using low angles X-ray powder diffraction; N_2 sorption at -196 °C; Diffuse Reflectance UV-Vis spectroscopy and High-Resolution Transmission Electron Microscopy coupled to Energy Dispersive X-Ray Analysis. Their electrochemical behaviour was investigated by Cyclic Voltammetry: a redox behaviour was observed only with a Fe content of 2.8 wt.%, likely due to Fe-oxyhydroxide clusters (FeOOH) at the nanotubes' outer surface.

Based on the electrochemical and physicochemical characterizations, nanocomposites of Fe-doped methylimogolite and reduced Graphene Oxide (rGO) were obtained for the first time through a simple method, previously developed by some of us to disperse electrochemically active nanomaterials onto carbon supports. In the micro/mesoporous nanocomposites (specific surface area in the 370 - 284 m^2 g^{-1} range) the NTs were highly dispersed within the 3D rGO matrix. Cyclic Voltammetry showed that the capacitive behaviour of the Fe-doped NTs alone were enhanced when they were embedded in the 3D rGO matrix.

1. Introduction

Methylimogolite (MeIMO) is a hybrid material with the chemical formula $(OH)_3Al_2O_3SiCH_3$, obtained for the first time by some of the authors of this manuscript (Bottero et al., 2011), occurring as single-walled nanotubes (NTs) characterized by a zig-zag configuration, as reported in an experimental and theoretical study by Monet et al. (Monet et al., 2018).

The hybrid NTs have a hydrophilic outer surface, lined by Al-(OH)-Al and Al-O-Al groups (Fernandez-Martinez and Michot, 2016) and an extremely hydrophobic inner surface, lined by Si-CH_3 groups: the latter is so hydrophobic that water molecules cannot diffuse within preformed MeIMO NTs, as previously shown by SAXS measurements (Nasi et al., 2020).

MeIMO NTs are obtained by a simple, one-pot sol-gel synthesis method (Bottero et al., 2011), and show potentialities in adsorption processes (Bottero et al., 2011; Nasi et al., 2020, Zanzottera et al., 2012a) and heterogeneous catalysis (Shafia et al., 2016; Bahadori et al., 2018). Indeed, the inner surface of MeIMO NTs is accessible to some molecules like methane (Bottero et al., 2011), dichloromethane (Nasi et al., 2020), bromopropanol (Amara et al., 2015) and Nile Red (Picot et al., 2019). The outer surface bears the acid/base properties of proper imogolite NTs, the parent nanomaterial with the chemical formula $(OH)_3Al_2O_3SiOH$, as confirmed by the interaction with some probe molecules like carbon dioxide (Zanzottera et al., 2012a), carbon monoxide, ammonia and water vapour (Bonelli et al., 2013a). Imogolite belongs to the allophane family, occurs naturally in volcanic soils,(Yoshinaga and Aomine, 1962) but may be also obtained through sol-gel synthesis (Farmer and Fraser, 1978; Wada et al., 1979; Bonelli et al., 2009). Conversely to MeIMO, proper imogolite is characterized by an extremely hydrophilic inner surface, lined by silanol groups, as shown by both experimental (Bonelli et al., 2009) and theoretical studies (Creton et al., 2008). Drying procedures of proper imogolite NTs may even lead to a deformation of the NTs, as shown in a recent experimental and theoretical study (D'Angelo et al., 2023).

Imogolite-like NTs organise into bundles having a pseudo-hexagonal arrangement: Scheme 1 reports, as an example, a sketch of two bundles of imogolite-like NTs to show the three families of pores occurring in the powder. Such arrangement of NTs allows the formation of B and C pores, in addition to the proper NTs' pores, namely the A pores, according to the nomenclature proposed by Ackerman (Ackerman et al., 1993). The A pores are, in turn, characterized by a diameter of ca. 10 Å and 20 Å in imogolite (Ackerman et al., 1993) and MeIMO (Bottero et al., 2011), respectively. The pores among three aligned NTs in a bundle (B pores) have a diameter of ca. 3.0 Å and 4.5 Å in imogolite and MeIMO, respectively. Finally, the slit mesopores among bundles (C pores) have a broader diameter distribution and have been found to be accessible to larger molecules/ions in both imogolite (Ackerman et al., 1993) and MeIMO (Nasi et al., 2020), providing a surface that can be easily functionalized (Zanzottera et al., 2012c) to enhance the possible applications of the NTs in adsorption/desorption processes, for instance.

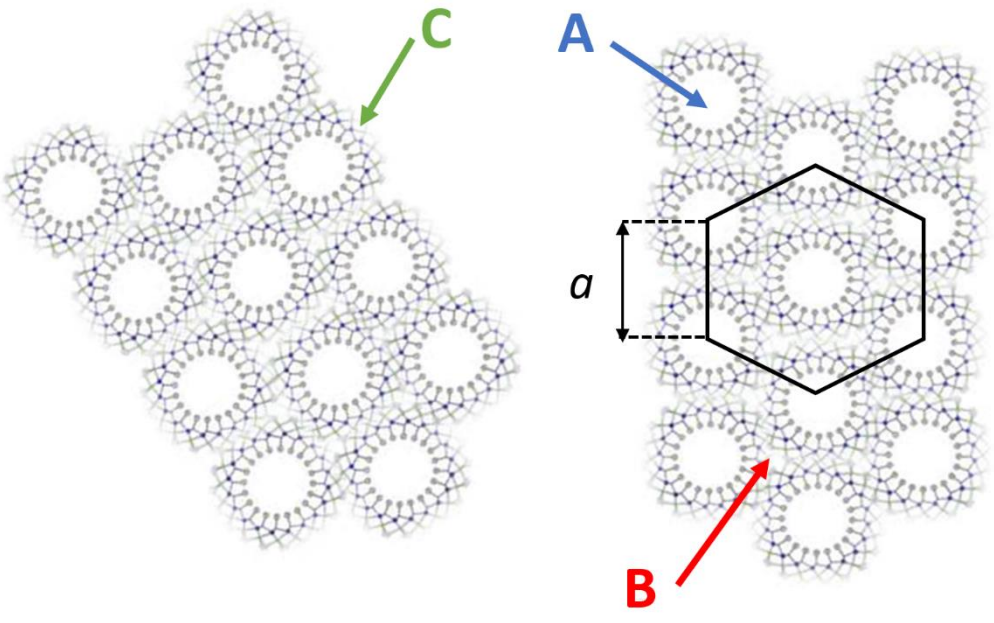

Scheme 1. Sketch of two bundles of imogolite-like NTs and their pseudo-hexagonal arrangement in powder form (adapted from Ackerman et al. (Ackerman et al., 1993)). The *a* parameter is the centre-to-centre distance between two adjacent NTs.

As compared to imogolite NTs, the synthesis of MeIMO has a higher yield and leads to bundles of aligned NTs (Bottero et al., 2011), which are also characterized by higher thermal stability, larger pore volume and surface area than imogolite NTs (Bonelli et al., 2009).

Concerning the C pores, and the related accessible surface, it has been already shown that octahedral Al^{3+} ions at the outer surface of both MeIMO and imogolite NTs can be isomorphically substituted by ions with a proper charge-to-radius ratio, like Fe^{3+}, by either direct synthesis (i.e. by adding $FeCl_3 \cdot 6H_2O$ to the mixture of the aluminium and silicon precursors) or post-synthesis ionic exchange with $FeCl_3 \cdot 6H_2O$ in water (Shafia et al., 2015, 2016; Bahadori et al., 2018). The following reaction occurs (eq. 1):

$$[Al(OH)Al]_{(s)} + Fe(H_2O)_6^{3+} \rightarrow [Fe(OH)Al]_{(s)} + Al(H_2O)_6^{3+} \qquad (1)$$

In a previous paper concerning the preparation of Fe-doped MeIMO with a maximum Fe content of 1.4 wt.%, it has been shown that isomorphic substitution of Al^{3+} at the outer surface of the NTs can be easily obtained by post-synthesis ionic exchange: the latter is a simpler procedure and could be used to introduce higher Fe contents as compared to direct synthesis (Bahadori et al., 2018).

The Fe-doped MeIMO NTs, already tested in the partial oxidation of tartrazine by H_2O_2 under UV illumination, were stable to Fe leaching in water (Bahadori et al., 2018) while catalysing a photo-Fenton reaction. Therefore, our curiosity arose about their possible redox behaviour. Indeed, several authors have shown that when the total Fe content exceeds 1 wt. % (Shafia et al., 2015), Fe doping of both MeIMO (Bahadori et al., 2018) and imogolite NTs (Shafia et al., 2016) leads to both Al^{3+}/Fe^{3+} isomorphic substitution and formation of Fe oxyhydroxide (FeOOH) clusters, mostly located at the

NTs outer surface (Shafia et al., 2016; Bahadori et al., 2018), due to the natural tendency of Fe to form Fe-O-Fe bridges (Wang et al., 2002). Moreover, other authors have recently explored the electrochemical potentialities of Fe-doped imogolite NTs: the latter were able to increase the available surface area of an electrode and enhance oxygen reduction reaction when Fe phthalocyanines were adsorbed on the NTs (Castro et al., 2016), showing that imogolite-like nanomaterials have some electrochemical potentialities, yet partially unexplored.

In this work, the FeOOH clusters were obtained on purpose, to have highly dispersed species, amenable to a redox behaviour, decorating the outer surface of NTs: the FeOOH/NTs interaction is expected to prevent cluster aggregation, as well as Fe leaching (Bahadori et al., 2018), i.e., two phenomena that could negatively affect the redox response of the nanomaterial. In previous work, we have shown that H_2O molecules cannot enter the extremely hydrophobic inner surface of MeIMO NTs, even when the powder is resuspended in liquid water (Nasi et al., 2020). To obtain FeOOH-decorated NTs, we adopted an ionic exchange procedure in water with Fe contents of either 1.4 or 2.8 wt. %. Noticeably, the latter content is twice the amount of Fe that can be obtained by direct synthesis, while still preserving the NTs (Bahadori et al., 2018). To follow a possible effect of the ionic exchange procedure on the FeOOH clusters' growth, ionic exchange was performed either by contacting preformed MeIMO NTs with a 2.8 wt.% Fe aqueous solution or by a two-step exchange procedure with two (fresh) 1.4 wt.% Fe solutions.

The NTs were characterized by complementary physicochemical techniques, namely low angles X-ray powder diffraction (to study the supramolecular order of NTs forming bundles in the obtained powder), N_2 sorption at – 196 °C (to determine NTs specific surface area and porosity), Diffuse Reflectance UV-Vis spectroscopy (to identify both isomorphically substituted Fe^{3+} species and FeOOH clusters), and High-Resolution Transmission Electron Microscopy (HRTEM) analysis, including EDX elemental mapping, to identify the Fe-containing sites and how they decorate the outer surface of the NTs. The redox behaviour of Fe-related species was studied by Cyclic Voltammetry.

Finally, to improve the NTs' electrochemical response, nanocomposites have been obtained with reduced Graphene Oxide (rGO) by slightly modifying (the employed synthesis process is reported in the experimental section, paragraph *2.1.2*) a procedure already adopted by some of the authors of this manuscript to produce nanocomposites of rGO with other types of electrochemically active compounds (Gigot et al., 2016), suitable for application in energy storage devices (Han et al., 2014).

Since many years, graphene aerogels, variously synthesized (e.g., rGO aerogels), have attracted a lot of interest (Gorgolis and Galiotis, 2017). Such carbonaceous 3D scaffolds have fascinating properties, namely the very low density, the high surface area, the thermal resistance and adsorption capacity, the high mechanical strength and electrical conductivity, and in particular, the capability to produce the so-called electrochemical double-layer capacitance (EDLC) (Wang et al., 2021). The intrinsic physico-chemical properties of rGO (and GO) are widely exploited in multiple applications. Moreover, rGO (and GO) properties are enhanced within composites, for instance with metal oxides, and are particularly interesting in the field of electrochemistry (supercapacitors) and catalysis (Tamang et al., 2023). Therefore, after a thorough characterization by Field Emission Scanning Electron Microscopy (FESEM), HRTEM analysis and N_2 sorption at – 196°, the rGO/NTs redox behaviour of the nanocomposite of rGO and the NTs at 2.8 wt.% Fe has been assessed by Cyclic Voltammetry and compared to that of Fe-doped NTs. This is the first report on the synthesis, physicochemical and electrochemical characterization of Fe-doped methylimogolite and its nanocomposites with rGO.

2. Experimental

2.1 Materials

If not otherwise specified, ACS-grade chemicals were employed (Sigma-Aldrich, Italy).

The Graphene Oxide powder (Single Layer GO, 0.7-1.2 nm) was purchased from Cheap Tubes Inc. – USA).

2.1.1 Synthesis and Fe-doping of MeIMO NTs

MeIMO NTs were synthesised according to the method developed by Bottero et al. (Bottero et al., 2011), by using triethoxymethylsilane (TEMS, 99 %) and aluminium tri-*sec*-butoxide (ATSB, 97%) as Si and Al sources, respectively, in 80 mM $HClO_4$ solution.

Fe-doped MeIMO NTs with either 1.4 wt.% or 2.8 wt.% Fe (chemical formula: $(OH)_3Al_{2-x}Fe_xO_3SiCH_3$ with x = 0.05 and 0.1, respectively) were obtained by post-synthesis ionic exchange, contacting a preformed MeIMO powder with an aqueous solution of $FeCl_3 \cdot 6H_2O$ (Bahadori et al., 2018). In a typical synthesis, proper amounts of Me-IMO and $FeCl_3 \cdot 6H_2O$ (97 %) were suspended in water (resulting pH $\leq$ 4.0) and maintained under stirring for 24 h. The solid was, then, filtered, washed, and dried in an oven at 50 °C overnight. Chemical analysis of the transparent supernatant solution did not detect the presence of residual iron with all the Fe-doped samples. The resulting sample at 1.4 wt.% Fe will be referred to as Fe1.4-MeIMO.

To study the possible effects of the ionic exchange conditions on the growth of the FeOOH clusters, two samples were obtained at 2.8 wt.% Fe). The former was obtained by contacting the preformed MeIMO powder with a 2.8 wt.% Fe solution, as described above (sample Fe2.8-MeIMO); ii) the latter was obtained by contacting the preformed MeIMO powder with a 1.4 wt.% Fe solution, filtrating and contacting the obtained solid with another 1.4 wt.% Fe fresh solution (Fe1.4x2-MeIMO).

2.1.2 Preparation of the rGO/NTs composites

rGO/NTs composites were produced by mixing two slurries: the former was obtained by dispersing commercial GO in water (2 mg mL^{-1}), as reported in ref (Gigot et al., 2016) for the fabrication of hybrid aerogels; the latter was obtained by dispersing either the Fe1.4-MeIMO or the Fe2.8-MeIMO NTs in water (0.6 mg mL^{-1}). Before mixing, each slurry was soaked for 5 h to increase the powder's wettability. The dispersion obtained by mixing the two slurries (where the Fe-doped NTs content was 23 wt.%) was sonicated for 5 min, transferred into a Teflon reservoir placed in a stainless-steel autoclave and heated at 180 °C in an oven for 12 h, to attain hydrothermal reduction of GO to rGO. The so-produced self-standing rGO hydrogel, embedding the Fe-doped-MeIMO NTs, was fast-cooled in liquid N_2 to allow water removal by ultrafast freeze-drying at – 50 °C and residual pressure of 50 mbar for 12 – 24 h. (Gigot et al., 2016) The obtained nanocomposites will be referred to as rGO/Fe1.4-MeIMO and rGO/Fe2.8-MeIMO.

2.2 Methods

Powders X-ray Diffraction (XRD) patterns were measured in the 2.5 – 18 2θ angles range ('Xpert Diffractometer using Cu K_α radiation, λ = 1.5415 Å, step width = 0.026 2θ, time per step 2.00 s).

N_2 adsorption/desorption isotherms were measured at -196 °C (Quantachrome Autosorb 1C) on powders previously outgassed either at 250 °C (NTs) or 150 °C (rGO/NTs nanocomposites) to remove water and other atmospheric contaminants, while preserving the NTs structure and the aerogel porous structure, respectively (Mackenzie, 1989; Zanzottera et al., 2012b).

Diffuse Reflectance (DR) UV-Vis spectra were measured on the NTs pre-outgassed at room temperature to remove moisture on a Cary 5000 UV–Vis-NIR spectrophotometer (Varian instruments) equipped with a DR sphere.

Electron micrographs were obtained on a high-resolution transmission electron microscope (HRTEM, Jeol 3010-UHR) operating at 300 kV, equipped with a LaB_6 filament and an Oxford Inca Energy TEM 300 EDS X-ray analyser (Oxford Link) for atomic recognition. Digital micrographs were acquired by an Ultrascan 1000 CCD camera and processed by Gatan digital micrograph. Before measurements, the as-received powder samples were grounded in an agate mortar and deposited on a copper grid covered with a lacey carbon film. Histograms of the size distribution of the Fe-containing clusters were obtained by considering a statistically representative number of nanoparticles on the HRTEM images and the mean particle diameter (d_m) of each distribution was calculated according to eq. 2:

$$d_m = \Sigma d_i n_i / \Sigma n_i \quad (2)$$

where n_i is the number of particles of diameter d_i.

The nanocomposite morphology was analysed by using a Field Emission Scanning Electron Microscope (FESEM Supra 40 manufactured by ZEISS), equipped with an Oxford Si(Li) detector for Energy Dispersive X-ray analysis (EDX). The samples were observed in their as-prepared form and no metallization was performed to avoid any surface-morphology modification.

The electrochemical characterization of the Fe-doped and undoped MeIMO together with the rGO/Fe2.8MeIMO was performed by using a potentiostat/galvanostat Metrohm Autolab M304 in an electrochemical cell made of three electrodes in which the reference electrode was an Ag/AgCl electrode, the counter electrode was platinum and the working electrode consisted of a glassy carbon electrode of 3 mm diameter covered by the MeIMOs. The measurements were performed in 2.0 M KOH saturated with nitrogen during the duration of the experiment. Cyclic voltammetry was performed in the whole potential range of the materials avoiding the evolution of gases.

3. Results and Discussion

213 *3.1 Physico-chemical characterization of MeIMO and Fe-doped MeIMO NTs*

214 Figure 1 reports the low-angle XRD patterns (section a) and the N_2 isotherms at -196 °C
215 (section b) of the undoped and Fe-doped NTs. MeIMO (black curve in Figure 1a) shows the typical
216 XRD patterns of NTs forming bundles in a pseudo-hexagonal arrangement (Bottero et al., 2011). The
217 most intense peak at 3.53 2θ is due to the d_{100} reflection, from which the parameter *a* corresponding
218 to the centre-to-centre distance between two aligned NTs within a bundle (Scheme 1) can be
219 calculated according to eq. 3:

220 $$a = 2d_{100}/\sqrt{3} \qquad (3)$$

221 which gives *a* = 28.9 Å for MeIMO. A shoulder to the main peak is observed at ca. 5.68 2θ, assigned
222 to the d_{111} reflection. Such a feature, i.e. a shoulder to the main peak of the d_{100} reflection, was already
223 observed in both natural (Wada et al., 1970) and synthetic imogolite NTs (Farmer and Fraser, 1978).
224 Several authors who studied proper imogolite NTs (Farmer and Fraser, 1978; Van Der Gaast et al.,
225 1985) assign such shoulder to the occurrence of a larger number of ordered NTs in a hexagonal close-
226 packed arrangement (Cradwick et al., 1972). Two (broader) peaks at higher 2θ values at ca. 9.03 and
227 12.38 2θ angles have been tentatively assigned to the NTs d_{001} and d_{211} reflections stemming from the
228 repetition of MeIMO structural units along the NTs, according to similar XRD diffraction of powder
229 samples of MeIMO obtained by the same procedure (Bottero et al., 2011). The peaks assignment is,
230 however, controversial, based on the recent literature reporting, *inter alia*, scattering experiments
231 with imogolite-like nanomaterials of various origins and compositions (Monet et al., 2018; D'Angelo
232 et al., 2023). Concerning the main peaks, modulations should be indexed with only two *hk* indices,
233 therefore, the first peak should be indexed as a 10 peak, the second peak as an 11 peak and the d_{001}
234 peak should be extinguished (Monet et al., 2018; D'Angelo et al., 2023).

235 The XRD pattern of the Fe1.4-MeIMO sample does not show substantial differences from
236 that of the parent MeIMO, in agreement with the limited Fe content (Bahadori et al., 2018).

Conversely, the two samples at 2.8 wt.% Fe have different XRD patterns, in that the d_{100} reflection shifts to higher 2θ values, becoming broader and more intense, finally hampering the calculation of the *a* parameter. This phenomenon can be ascribed to a change in the ordering of NTs upon ionic exchange with 2.8 wt.% Fe, which induces non-negligible changes in the alignment of the NTs in the final material in powder form, since the presence of Fe-oxyhydroxides species of different sizes (*vide infra*) at the outer surface of the NTs should perturb their successive organization into bundles when powders are obtained. The same phenomenon could also be responsible for the appearance of new pores, with a diameter of ca. 10 Å (*vide infra*), in the samples at 2.8 wt.% Fe. It must be remarked that the adopted XRD sample holder did not allow a more accurate determination of the d_{100} peak position (due to the small amount of the available powders at 2.8 wt.% Fe), however, the HRTEM inspection allowed us to infer more details about the formation of NTs bundles (*vide infra*).

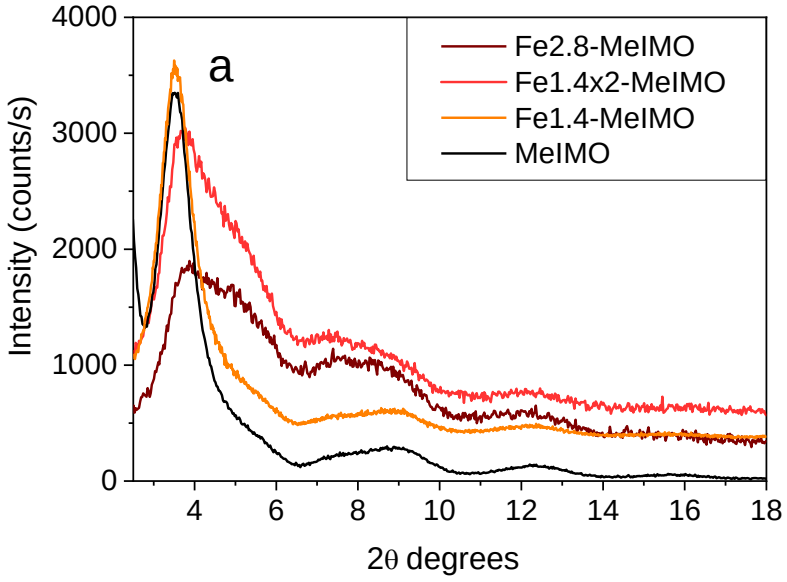
a
Fe2.8-MeIMO
Fe1.4x2-MeIMO
Fe1.4-MeIMO
MeIMO
Intensity (counts/s)
2θ degrees

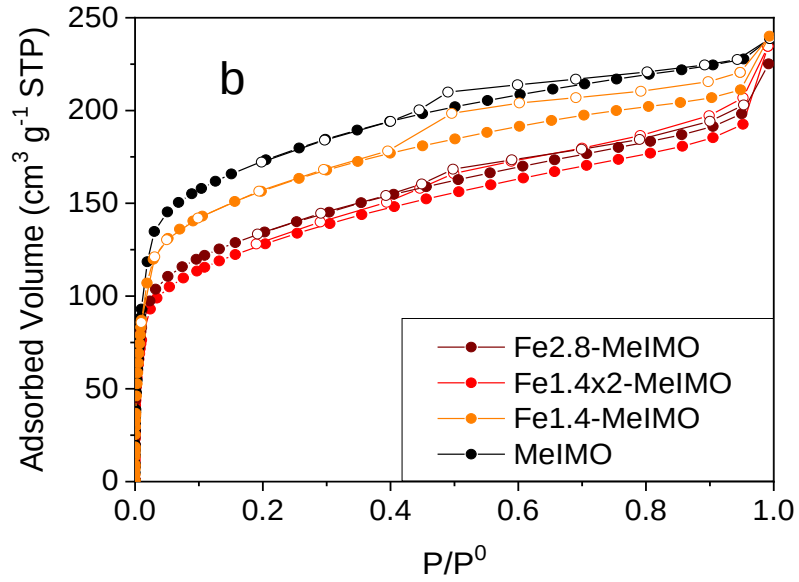
b
Fe2.8-MeIMO
Fe1.4x2-MeIMO
Fe1.4-MeIMO
MeIMO
Adsorbed Volume (cm3 g-1 STP)
P/P0

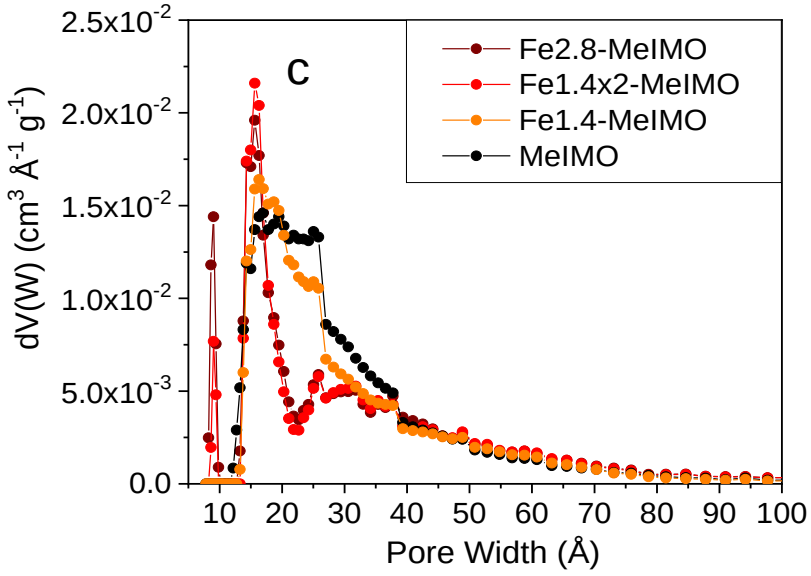
c
Fe2.8-MeIMO
Fe1.4x2-MeIMO
Fe1.4-MeIMO
MeIMO
dV(W) (cm3 Å-1 g-1)
Pore Width (Å)

Figure 1. Low angles XRD patterns (a), N_2 isotherms at -196 °C (b) and PSD curves (c) of the following samples: MeIMO (black curves), Fe1.4-MeIMO (orange curves), Fe1.4x2-MeIMO (red curves) and Fe2.8-MeIMO (brown curves).

Figure 1b reports the N_2 isotherms at -196 °C of both undoped and Fe-doped MeIMO NTs: the four samples show Type IV isotherms, proper of microporous materials with some mesoporosity (Armandi et al., 2008; Thommes et al., 2015). The H4 hysteresis loop observed in all the isotherms is typical of slit/wedge-shaped pores, likely forming among the bundles (Scheme 1). The values of Brunauer-Emmett-Teller Specific Surface Area (BET SSA) in Table 1 show that Fe-doping leads to a progressive, but limited, decrease of the SSA. The curves of the corresponding Pore Size Distribution (PSD) (Figure 1c) show that the nanomaterials' porosity is strongly affected by ionic exchange in different ways. Concerning mesopores, Fe-exchange brings about a decrease in the number of pores in the 20 – 40 Å range: indeed, the formation of Fe-oxyhydroxide clusters at the NTs outer surface could affect the (larger) mesopores occurring between bundles, namely the C pores in Scheme 1. Concerning micropores, at 2.8 wt.% Fe a new family of micropores shows up with a diameter of ca. 10 Å, which could be due to a "new" porosity, absent at lower Fe content, due to the occurrence of Fe-oxyhydroxide clusters at the outer surface of the NTs that affect the subsequent formation of bundles in the powder and the packing of the Fe-doped NTs at higher Fe content.

Fe doping leads to a slight decrease in the samples' microporous volume, with the likely exception of the Fe2.8-MeIMO sample. The difference in the microporous volume between the two samples at 2.8 wt.% Fe (Fe14x-MeMO and Fe2.8-MeIMO) may indicate that the two synthesis procedures slightly affect the samples' textural properties, although they could also lead to different clusters' growth, which was further investigated by HRTEM (*vide infra*).

Table 1. Nominal Fe content, relevant textural properties, and bandgap energy (E_g, eV) of the studied samples.

Sample (Nominal wt.% Fe)	Chemical formula	BET SSA ($m^2\ g^{-1}$)	Total pore volume ($cm^3\ g^{-1}$)	Bandgap energy (eV)[b]
		Micropore area[a] ($m^2\ g^{-1}$)	Micropore volume[a] ($cm^3\ g^{-1}$)	
MeIMO (0)	$(OH)_3Al_2O_3SiCH_3$	615	0.35	4.9
		336	0.14	
Fe1.4-MeIMO (1.4)	$(OH)_3Al_{1.95}Fe_{0.05}O_3SiCH_3$	560	0.33	2.4
		240	0.10	
Fe1.4x2-MeIMO (2.8)	$(OH)_3Al_{1.9}Fe_{0.1}O_3SiCH_3$	455	0.29	2.3
		217	0.09	
Fe2.8-MeIMO (2.8)	$(OH)_3Al_{1.9}Fe_{0.1}O_3SiCH_3$	478	0.31	2.3
		245	0.16	

[a] As determined by applying the *t*-plot method.

[b] As determined by applying the Tauc plot method for an indirect semiconductor to the DR-UV-Vis spectra.

Further insight into the effect of Fe-doping can be derived by the DR UV-Vis spectra reported in Figure 2: MeIMO (black curve) has, as expected, a negligible absorption in the UV-vis range, whereas the Fe-doped samples show intense and broad absorption bands both below and above 300 nm. Below 300 nm, two bands at ca. 235 and 290 nm are ascribed to charge transfer (CT) transitions from O^{2-} to isolated Fe^{3+} ions, as observed in other Fe-doped alumino-silicate systems, namely Fe-exchanged zeolites (Kumar et al., 2006; Iwasaki et al., 2008; Ma et al., 2012).

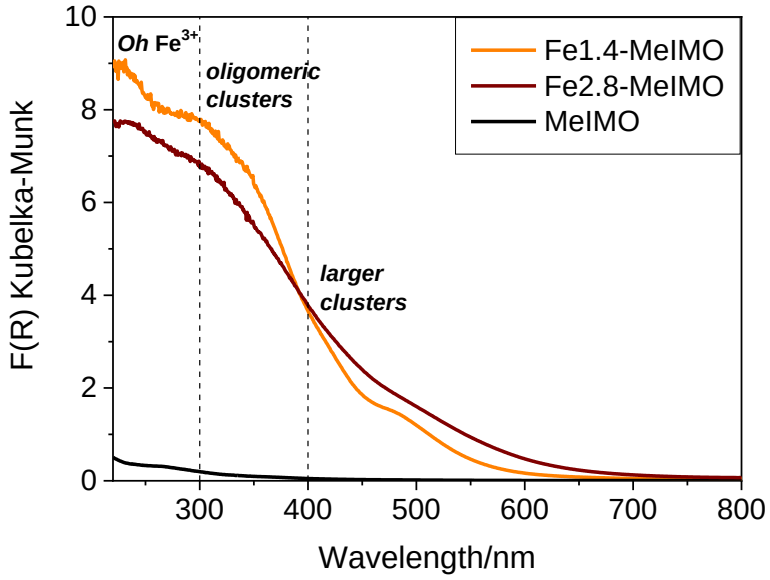

Figure 2. DR UV-Vis spectra of the following samples: MeIMO (black curve), Fe1.4-MeIMO (orange curve) and Fe2.8-MeIMO (brown curve).

At variance with zeolites, the formation of tetrahedral Fe^{3+} sites (band at 235 nm) is unlikely here, and both bands are assigned to Fe^{3+} ions in likely octahedral (*Oh*) coordination. Indeed, the conditions adopted during the ionic exchange in water lead us to exclude the assignment of the band at 235 nm to CT to tetrahedral Fe^{3+} species, although previous calculations on similar systems showed that they could occur as defects at the inner and outer surface of the NTs (Teobaldi et al., 2008). Therefore, the 235 nm band can be due to some Fe^{3+} in defective sites, i.e. in a different environment as compared to the *Oh* species deriving from reaction (1), absorbing at 290 nm. The absorption above 300 nm is complex. According to the literature, Fe oxyhydroxide clusters of different dimensions absorb at different wavelengths (Kumar et al., 2006; Iwasaki et al., 2008; Ma et al., 2012; Bahadori et al., 2018). More specifically, larger clusters absorb above 400 nm, therefore bands in the 300–400 nm range are assigned to CT transitions in smaller (oligomeric) Fe oxyhydroxide clusters, whereas bands above 400 nm are ascribed to larger (nm range) Fe oxyhydroxide particles and *d*-*d* transitions

(Kumar et al., 2006; Iwasaki et al., 2008; Ma et al., 2012; Bahadori et al., 2018). Interestingly, the bands have different relative intensities with the samples (the spectrum of the Fe1.4x2-MeIMO sample was practically superimposable to that of Fe2.8-MeIMO and was not reported for clarity). Accordingly, at higher Fe content, the bands due to oligomeric species become less intense, whereas the absorption due to larger clusters increases in intensity and becomes broader.

By applying Tauc's plot method, the NTs bandgap energy values in Table 1 have been determined. As expected, MeIMO is an insulator, with a bandgap of 4.9 eV, in agreement with theoretical results (Alvarez-Ramírez, 2009), but doping with Fe turns the NTs into a semiconductor with a bandgap of 2.3 - 2.4 eV. Interestingly, increasing the Fe content to 2.8 wt.% does not contribute to a remarkable decrease in the bandgap, as compared to 1.4 wt. % Fe. As demonstrated by several authors (Avellan et al., 2014; Shafia et al., 2015; Bahadori et al., 2018), the isomorphic substitution of Al^{3+} by Fe^{3+} in imogolite-like NTs hardly exceeds 1.0 wt.% Fe. However, increasing the Fe content could affect the growth of the Fe-oxyhydroxide clusters. Consequently, the bandgap energy decreases to a certain extent, due to the Al^{3+}/Fe^{3+} isomorphic substitution, but higher Fe contents mainly lead either to the growth of preformed Fe-oxyhydroxide clusters or to the growth of new clusters around isomorphically substituted Fe^{3+} sites, acting as "crystalline seeds".

To unravel the effect of Fe-doping on the growth of Fe-containing species as a consequence of the different ionic exchange procedures, a careful HRTEM characterization combined with EDX analysis was carried out on both the Fe1.4x2-MeIMO and Fe2.8-MeIMO samples.

Concerning morphology, in a previous paper (Bottero et al., 2011) it was shown that MeIMO forms bundles of closely packed NTs. First, independently from the Fe amount and the adopted doping procedure, the morphological features of bare MeIMO NTs were maintained upon Fe insertion (Figures 3 and 4). Moreover, Fe species, likely Fe-oxyhydroxide clusters, were observed at the outer surface of the NTs (indicated by arrows in Figures 3a, 3d, and Figures 4a, 4b) and no cluster agglomerates were observed. The clusters' size was evaluated by considering electron micrographs

346 acquired at least at 50,000× magnification, where the Fe-oxyhydroxide clusters, well contrasted as
347 compared to the MeIMO structure, were detected. Highly dispersed Fe-containing species were
348 observed in both samples, having a mean diameter d_m= 4.9 ± 0.9 nm in Fe1.4x2-MeIMO and d_m= 5.1
349 ± 0.8 nm in Fe2.8-MeIMO. This fact agrees with the DR UV-Vis spectra (Figure 2), showing the
350 occurrence of both oligomeric and larger FeOOH clusters. Despite the similar mean diameters of the
351 clusters, their size distribution was broader with the Fe1.4x2-MeIMO sample (ranging between 2 and
352 9 nm) as compared to the Fe2.8-MeIMO sample (ranging from 3 to 8 nm). These features indicate
353 that the adopted doping procedures did not affect much the average size of the clusters, but the double
354 exchange procedure led to a broader size distribution of the latter species. Moreover, it may indicate
355 that if the double exchange is carried out, besides increasing the size of pre-formed clusters, new
356 clusters form, confirming that it is very difficult to control the extent of isomorphic substitution versus
357 cluster growth, as both processes unavoidably occur by ionic exchange.

358

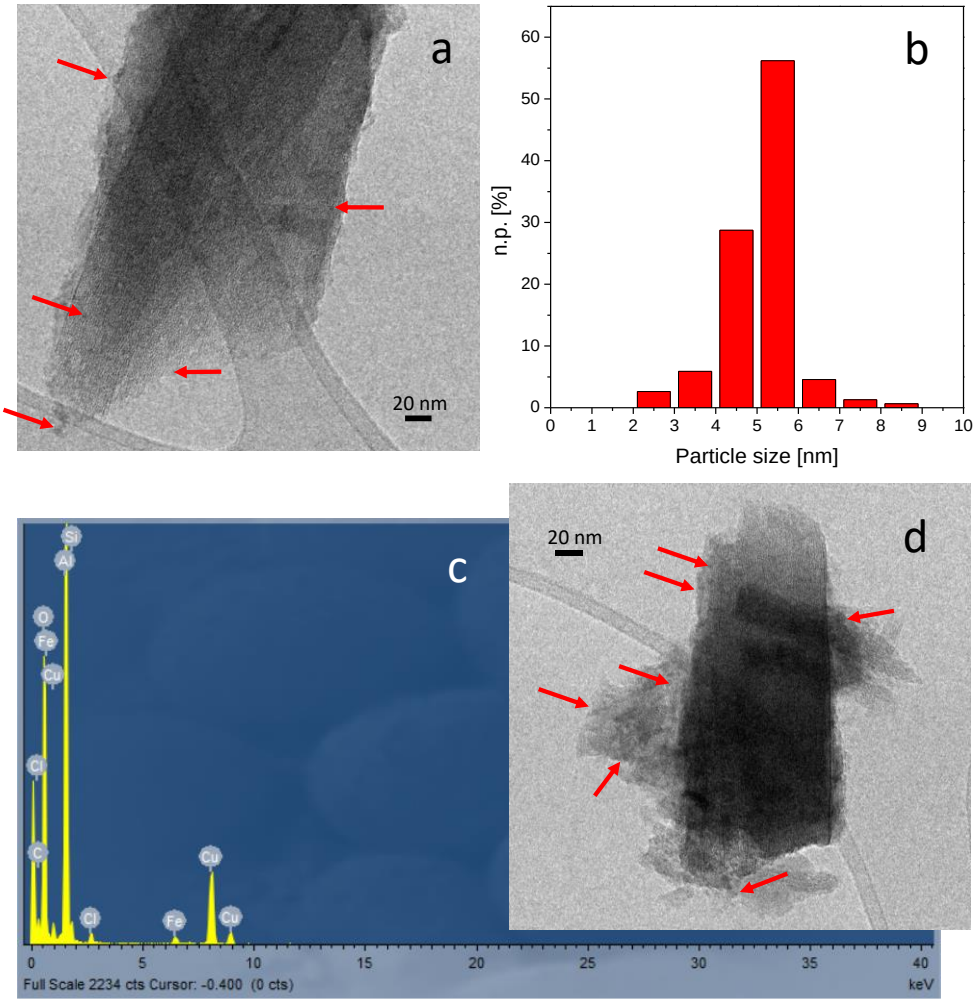

359

360 **Figure 3.** HRTEM representative images of Fe1.4x2-MeIMO in which the bundles formed by parallel
361 NTs can be observed (a, d). Particle size distribution of Fe oxo-hydroxide clusters (b) and EDX
362 spectrum of the region shown in d (c). Instrumental magnification 50,000×. The Fe-containing species
363 are highlighted by red arrows. In the EDX spectrum, the lines of Cl and Cu are due to the adopted Fe
364 precursor and the sample holder, respectively.

365

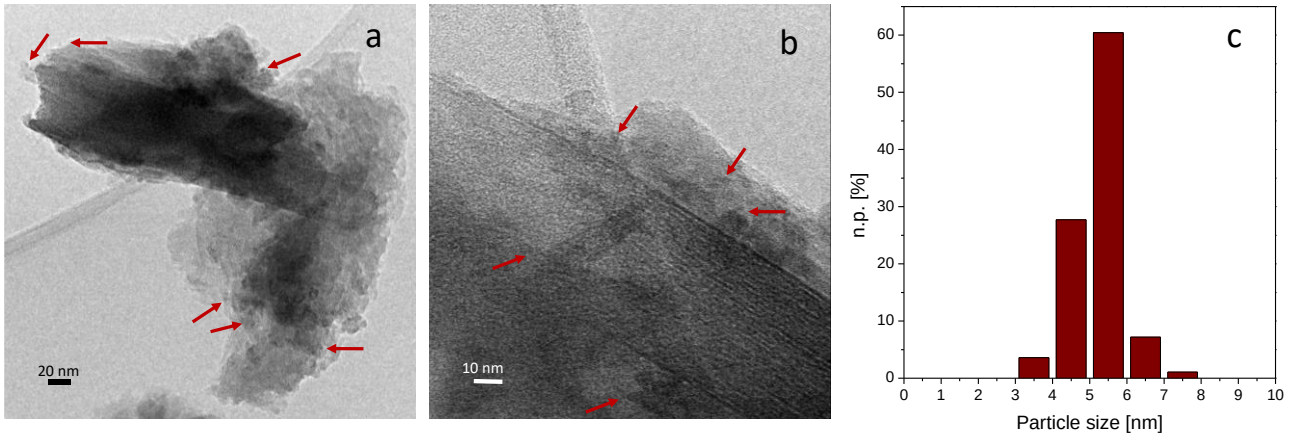

Figure 4. HRTEM representative images of Fe2.8-MeIMO bundles (a) formed by parallel NTs (b). Particle size distribution of Fe oxo-hydroxide clusters (c). Instrumental magnification is 50,000× and 150,000×, respectively. The Fe-containing species are highlighted by brown arrows.

3.2 Physico-chemical characterization of the rGO/NTs nanocomposites

On the ground of the previously described physicochemical characterization, rGO/NTs nanocomposites were produced with the Fe1.4-MeIMO and the Fe2.8-MeIMO samples. Figure 5 reports some selected micrographs obtained by FESEM inspection of the parent rGO and the rGO/Fe1.4-MeIMO nanocomposite: in Figure 5a, wrinkled and curled-up rGO flakes, typical of the adopted preparation procedure (Gigot et al., 2016), are observed, giving rise to a 3D highly porous morphology, as it can be appreciated both at higher and lower magnification (inset). The occurrence of NTs interacting with the rGO matrix may be appreciated in Figure 5b, showing a good dispersion of the NTs, likely aggregated in bundles, within the rGO flakes, both at higher and lower (inset) magnification.

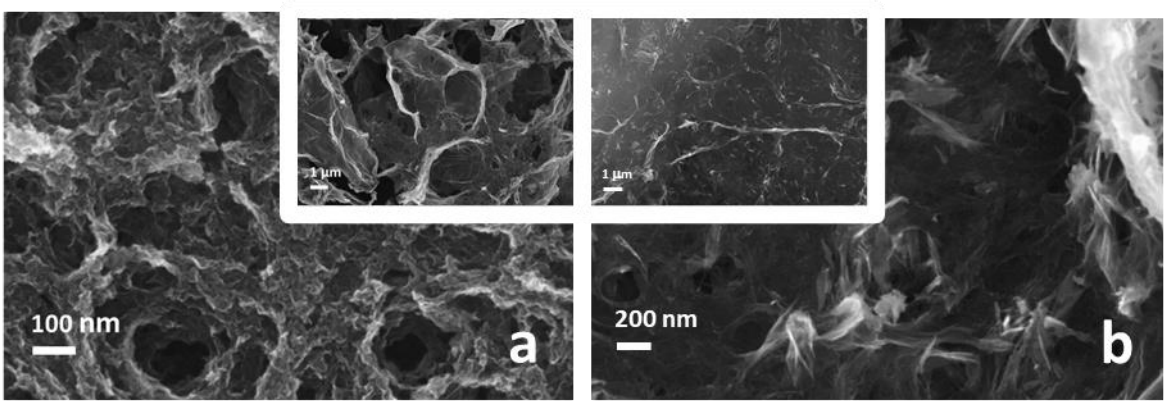

Figure 5. Selected FESEM micrographs of the parent rGO (a) and the rGO/Fe1.4-MeIMO nanocomposite (b).

The interaction between the Fe2.8-MeIMO NTs and rGO was further verified by HRTEM measurements on the rGO/Fe2.8-MeIMO nanocomposite (Figure 6), which put in evidence that the NTs bundles and rGO are finely inter-dispersed, as also confirmed by EDX analysis (data not shown). In this case, at variance with what was previously observed with the Fe1.4x2-MeIMO and Fe2.8-MeIMO samples, the NTs were prevalently embedded within the rGO matrix, mostly as bundles or aggregates of bundles, in agreement with the adopted synthesis procedure. Figure 6a shows very likely aggregates of bundles embedded in the rGO, whereas Figure 6b allows appreciating bundles of NTs dispersed in the rGO matrix.

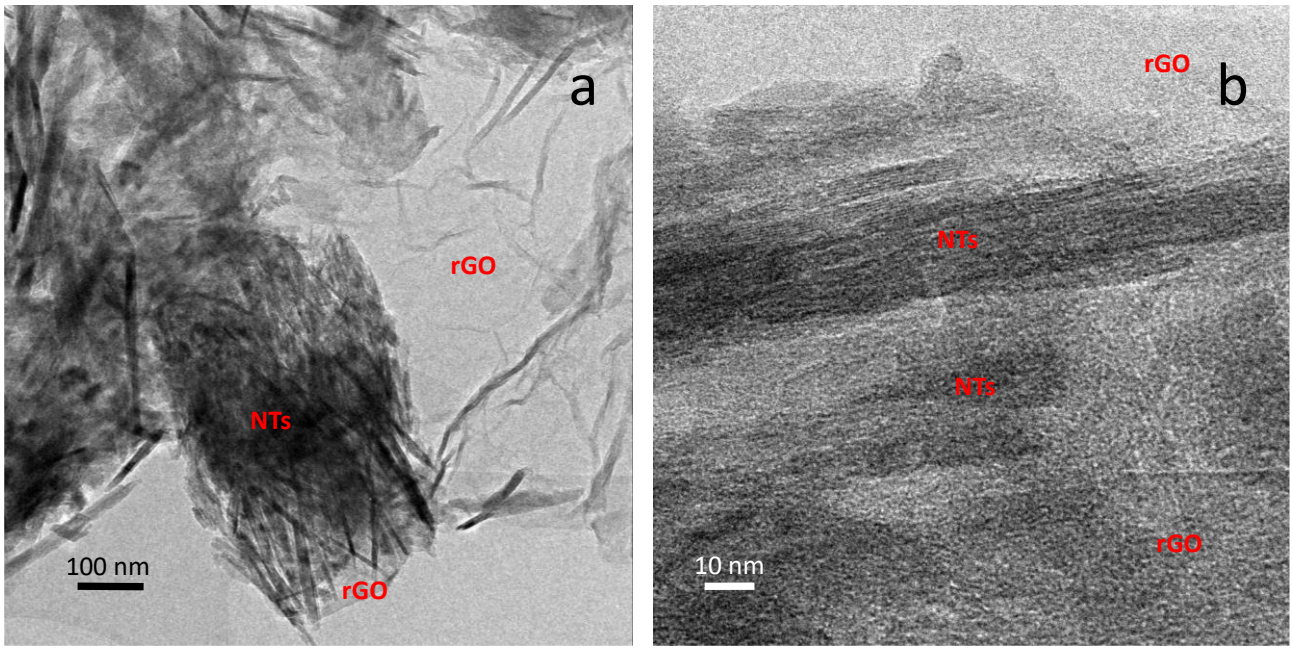

Figure 6. Representative HRTEM images of the rGO/Fe2.8-MeIMO nanocomposite at low (a) and high magnification (b) in which the NTs appear as enveloped by the rGO flakes. Instrumental magnification is 50,000× and 150,000×, respectively.

The effect of the Fe-doped MeIMO NTs on the porous structure of rGO was also assessed by measuring their N_2 isotherms at - 196 °C (Figure 7). The isotherm of the pristine rGO aerogel shows an adsorption branch composed of Type I(b) (low P/P^0 region, associated with micropores filling) and Type IV (high P/P^0 region, associated with mesopores filling) isotherms, with a limited hysteresis loop. The latter shows a lower limit of the desorption branch located at the cavitation-induced P/P^0 (ca. 0.4) and is likely given by non-rigid aggregates of rGO sheets (Gigot et al., 2016). A similar isotherm shape is observed with the rGO/Fe1.4-MeIMO nanocomposite, but in this case, a more complex hysteresis loop is present, as given by the overlapping of the two loops, specific to each parent nanomaterial. In contrast, the rGO/Fe2.8-MeIMO nanocomposite shows a very limited hysteresis loop (as also observed in the Fe2.8-MeIMO NTs alone). The fine dispersion of NTs bundles within the rGO matrix (as evidenced by HRTEM) could contribute to this feature.

The NTs addition to rGO brings about a decrease of the BET SSA, from 458 m^2g^{-1} (pristine rGO aerogel) to 370 and 284 m^2g^{-1} (rGO/Fe1.4-MeIMO and rGO/Fe2.8-MeIMO, respectively). The decrease in surface area is accompanied by a decrease in total porous volume and microporous volume (Table 2). This feature, apparently in contrast to the high SSA of the parent Fe-doped NTs, is mainly due to the lower outgassing temperature adopted with the studied aerogels. As reported in the Experimental Section, to preserve the porous architecture of the freeze-dried aerogels, an outgassing temperature of 150°C was adopted, whereas in previous work it was shown that both SSA and total pore volume of Me-IMO NTs are halved when the outgassing temperature is lowered from 300 to 150°C (Bottero et al., 2011).

Table 2. BET SSA and micropore area ($m^2\,g^{-1}$), total pore volume and micropore volume ($cm^3\,g^{-1}$) of rGO aerogel and the rGO/NTs nanocomposites as derived from N_2 sorption isotherms at -196 °C.

Sample	**BET SSA ($m^2\,g^{-1}$)**	**Total pore volume ($cm^3\,g^{-1}$)**
	Micropore area ($m^2\,g^{-}$	**Micropore volume ($cm^3\,g^{-1}$)**
rGO	458	0.45
	139	0.08
rGO/Fe1.4-MeIMO	370	0.53
	117	0.05
rGO/Fe2.8-MeIMO	284	0.33
	60	0.03

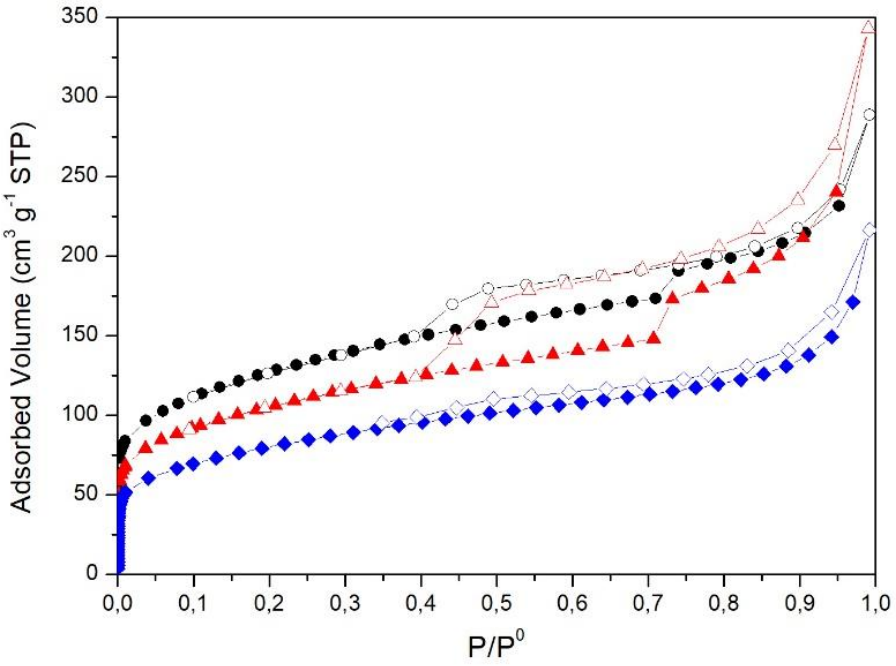

Figure 7. N_2 isotherms at -196 °C of pristine rGO (black circles), rGO/Fe1.4-MeIMO (red triangles) and rGO/Fe2.8-MeIMO (blue diamonds).

3.3 Electrochemical characterization

Electrochemical measurements were carried out in a three-electrode cell, as described in the experimental section. Cyclic voltammetry was performed in 2.0 M KOH firstly at 2 mV s^{-1} until stable voltammograms have been obtained, and then at higher scan rates.

Figure 8a shows typical stable cyclic voltammograms obtained by sweeping the scan rate between 0.1 and -1.6 V vs Ag/AgCl: MeIMO produced the blue voltammogram, which is characterized by a fair capacitive behaviour, evidenced by the presence of the well-known rectangular hysteresis, but also a strong resistive behaviour, evidenced by the linearization and tilting of the voltammogram. Fe-doping produced an increase in the conductivity of the nanomaterial (by a reduction of the tilt angle, clearly seen with the Fe1.4-MeIMO sample) and a larger and more stable

capacitance, clearly seen in the almost constant anodic current onto which small redox peaks appear (as seen with the Fe2.8-MeIMO sample).

According to the literature (Xia et al., 2016), the observed peaks refer to the following Fe reversible redox processes (eq. 4-6):

$$Discharge: FeOOH + H_2O + e^- \rightarrow Fe(OH)_2 + OH^- \quad (4)$$

$$Charge: Fe(OH)_2 + OH^- \rightarrow FeOOH + H_2O + e^- \quad (5)$$

and/or

$$3\,Fe(OH)_2 + 2\,OH^- \rightarrow Fe_3O_4 + 4H_2O + 2\,e^- \quad (6)$$

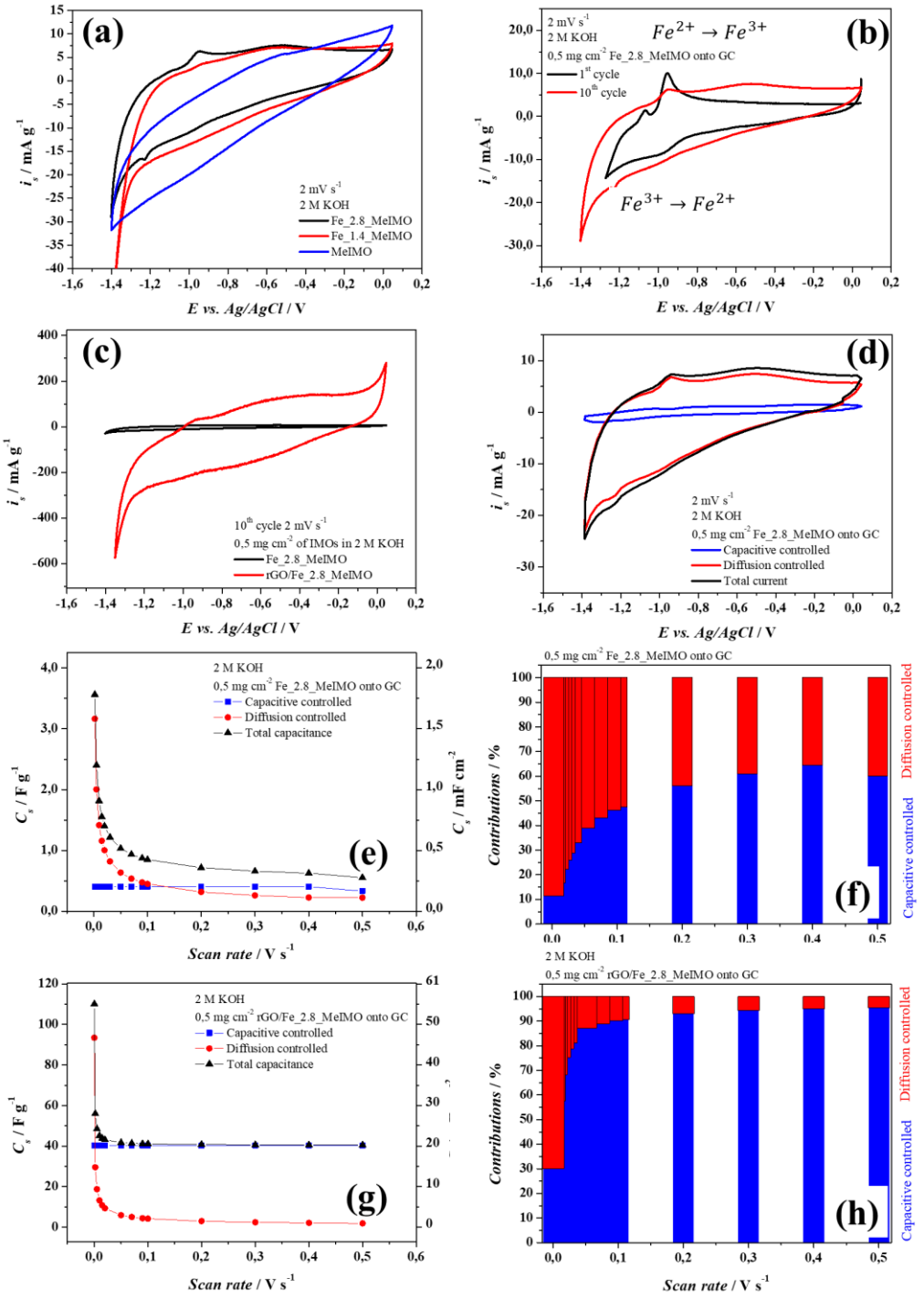

447

448 **Figure 8.** Section a): cyclic voltammetry at 2 mV s^{-1} recorded at the 10th cycle with the following
449 samples: Fe2.8MeIMO (black curve), Fe1.4MeIMO (red curve) and MeIMO (blue curve). Section
450 b): cyclic voltammetry recorded at the 1st cycle (black curve) and 10th cycle (red curve) with the
451 Fe2.8MeIMO sample. Section c): cyclic voltammetry recorded at the 10th cycle with the

Fe2.8MeIMO (black curve) and rGO/Fe2.8MeIMO nanocomposite (red curve). Sections d), e) and f) are those on the sample Fe2.8MeIMO and they show d) the reconstructed capacitive-controlled (blue curve) and diffusion-controlled (red curve) voltammetries compared to the raw data (black curve) estimated at 2 mV s^{-1}; e) the rate capabilities and f) the percentage of the capacitive-controlled and diffusion-controlled charges at different scan rates. Sections g) and h) show the rate capabilities and the percentage of the capacitive-controlled and diffusion-controlled charges at different scan rates for the rGO/Fe2.8MeIMO nanocomposite.

In Figure 8a, the stable cyclic voltammetry curves are reported, as obtained after 10 cycles. The first cycle appears, instead, quite different and both smaller capacitance (smaller hysteresis) and larger peaks are clear, as reported in Figure 8b. According to the literature, this phenomenon is an activation process from Fe_2O_3 to FeOOH described by eq. 7:

$$Fe_2O_3 + H_2O \rightarrow 2FeOOH \qquad (7)$$

Such an activation process is visible when cyclic voltammetry is performed on the Fe-doped MeIMO, but when the NTs are embedded in the 3D structure of rGO, the phenomenon is no more visible: in Figure 8c the voltammograms at the tenth cycle of the Fe2.8MeIMO sample and the rGO/Fe2.8MeIMO nanocomposite are compared, showing the enhancement of the capacitance of the latter sample at the electrode, in agreement with the fact that the CV plot of the bare rGO (not reported) showed a box-like shape, typical of the ideal capacitive behaviour of the material (Gigot et al., 2016).

The kinetic analysis performed on the Fe2.8MeIMO sample and the rGO/Fe2.8MeIMO nanocomposite allowed the appreciation of the effect that rGO made on the electrochemical behaviour of the Fe-doped MeIMO. According to Dunn's method (Wang et al., 2007), voltammograms acquired at different scan rates were analysed to retrieve the capacitive-controlled and diffusion-controlled

currents characteristic of each material. The current $i(V)$ at each scan rate (ν) therefore follows eq. 8 (Bard and Faulkner, 2000):

$$i(V) = k_a\nu + k_b\nu^{1/2} \qquad (8)$$

Figure 8d reports, as an example, the reconstructed voltammetry at 2 mV s^{-1} of the Fe2.8MeIMO sample showing the measured voltammetry (black curve), and the reconstructed voltammetry accounting for capacitive current (blue curve) and diffusion-controlled current (red curve) as calculated according to eq. 8. With the same code of colours, in Figures 8e-8h the rate capability test is presented as the usual plot of capacitance *versus* scan rate and as histograms, respectively, showing the percentage of capacitive-controlled and diffusion-controlled charges at each scan rate. By comparing this data analysis of the Fe2.8MeIMO sample with that of the rGO/Fe2.8MeIMO sample in Figure 8f and 8h, we can appreciate not only that the capacitance increases due to the presence of the rGO 3D structure, but also that the efficiency in the surface utilization of the Fe2.8MeIMO sample increases, leading to a clear enhancement of 1 order of magnitude (at 2 mV s^{-1}, from 3 to ≃90 F g^{-1}) of the diffusion-controlled charges, assuming that the totality of the current is produced by the Fe-doped MeIMO NTs alone.

Conclusions

Fe-doped methylimogolite NTs with an iron content of 1.4 and 2.8 wt.% were synthesized by following a simple ionic exchange procedure of preformed methylimogolite NTs in water suspension. In this way, FeOOH clusters decorating the outer surface of preformed NTs were obtained, showing a redox response as measured by Cyclic Voltammetry. The interaction with the NTs matrix allowed stabilization of the clusters and favoured their dispersion, preventing aggregation phenomena that could lower the electrochemical response.

Successively, rGO/Fe-doped NTs were obtained for the first time by a facile and environment-friendly hydrothermal process followed by a freeze-drying procedure, which allowed reaching an effective dispersion of the NTs among the rGO flakes interconnected each other in a 3D porous architecture, as testified by electron microscopies. This nanocomposite material clearly shows an enhanced electrochemical response, thanks to the cooperation between the rGO properties, widely exploited in the last decade in the production of electrodes for energy storage devices, and the redox properties of Fe-doped NTs of the imogolite type. The latter had been already studied in Fe-modified imogolite NTs (Castro et al., 2016), showing that electrodes modified with imogolite and Fe-modified imogolite showed an increased electrochemically-active surface area (increased capacitive current).

The nanocomposites developed in this work, offering chemical stability, high surface area and the possibility to stabilize electrochemically active Fe species, could become a platform on which to disperse/support several types of electrocatalysts (e.g., Fe phthalocyanines) for relevant reactions, like oxygen reduction, for instance.

Acknowledgements

Dr Roberto Nasi (Department of Applied Science and Technology, Politecnico di Torino) is acknowledged for performing the ionic exchange of the Fe1.4x2-MeIMO and the Fe2.8-MeIMO samples.

Dr Arnaud Gigot (Department of Applied Science and Technology, Politecnico di Torino) is acknowledged for contributing to developing and performing the hydrothermal process to obtain the Fe doped-MeIMO/rGO nanocomposites.

References

522 Ackerman, W.C., Smith, D.M., Huling, J.C., Kim, Y.W., Bailey, J.K., Brinker, C.J., 1993.
523 Gas/vapor adsorption in imogolite: a microporous tubular aluminosilicate. Langmuir 9,
524 1051–1057. https://doi.org/10.1021/la00028a029

525 Alvarez-Ramírez, F., 2009. First principles studies of Fe-containing aluminosilicate and
526 aluminogermanate nanotubes. J. Chem. Theory. Comput. 5, 3224–3231.
527 https://doi.org/10.1021/ct9004992

528 Amara, M.S., Paineau, E., Rouzière, S., Guiose, B., Krapf, M.-E.M., Taché, O., Launois, P.,
529 Thill, A., 2015. Hybrid, tunable-diameter, metal oxide nanotubes for trapping of organic
530 molecules. Chemistry of Materials 27, 1488–1494. https://doi.org/10.1021/cm503428q

531 Armandi, M., Bonelli, B., Karaindrou, E.I., Areán, C.O., Garrone, E., 2008. Post-synthesis
532 modifications of SBA-15 carbon replicas: Improving hydrogen storage by increasing
533 microporous volume. Catal. Today 138, 244–248.
534 https://doi.org/10.1016/j.cattod.2008.05.002

535 Avellan, A., Levard, C., Kumar, N., Rose, J., Olivi, L., Thill, A., Chaurand, P., Borschneck,
536 D., Masion, A., 2014. Structural incorporation of iron into Ge-imogolite nanotubes: a
537 promising step for innovative nanomaterials. RSC Advances 4, 49827–49830.
538 https://doi.org/10.1039/C4RA08840A

539 Bahadori, E., Vaiano, V., Esposito, S., Armandi, M., Sannino, D., Bonelli, B., 2018. Photo-
540 activated degradation of tartrazine by H_2O_2 as catalyzed by both bare and Fe-doped
541 methyl-imogolite nanotubes. Catal. Today 304, 199–207.
542 https://doi.org/10.1016/j.cattod.2017.08.003

543 Bard, A.J., Faulkner, L.R., 2000. Electrochemical methods: fundamentals and applications,
544 2nd Edition. ed.

545 Bonelli, B., Armandi, M., Garrone, E., 2013a. Surface properties of alumino-silicate single-
546 walled nanotubes of the imogolite type. Phys. Chem. Chem. Phys, 15, 13381–13390.
547 https://doi.org/10.1039/c3cp51508g

548 Bonelli, B., Bottero, I., Ballarini, N., Passeri, S., Cavani, F., Garrone, E., 2009. IR
549 spectroscopic and catalytic characterization of the acidity of imogolite-based systems. J.
550 Catal. 264, 15–30. https://doi.org/10.1016/j.jcat.2009.03.003

551 Bonelli, B., Zanzottera, C., Armandi, M., Esposito, S., Garrone, E., 2013b. IR spectroscopic
552 study of the acidic properties of alumino-silicate single-walled nanotubes of the imogolite
553 type. Catal. Today 218–219, 3–9. https://doi.org/10.1016/j.cattod.2013.02.004

554 Bottero, I., Bonelli, B., Ashbrook, S.E., Wright, P.A., Zhou, W., Tagliabue, M., Armandi, M.,
555 Garrone, E., 2011. Synthesis and characterization of hybrid organic/inorganic nanotubes
556 of the Imogolite type and their behaviour towards methane adsorption. Phys. Chem.
557 Chem. Phys. 13, 744–750. https://doi.org/10.1039/c0cp00438c

558 Bursill, L.A., Peng, J.L., Bourgeois, L.N., 2000. Imogolite : An aluminosilicate nanotube
559 material. Philos. Mag. A 80, 105–117. https://doi.org/10.1080/01418610008212043

560 Castro, C., Arancibia-Miranda, N., Acuña-Rougier, C., Escudey, M., Tasca, F., 2016.
561 Spectroscopic and electrochemical studies of imogolite and Fe-modified Imogolite
562 nanotubes. Nanomaterials 6(2), 28. https://doi.org/10.3390/nano6020028

563 Cradwick, P.D.G., Farmer, V.C., Russell, J.D., Masson, C.R., Wada, K., Yoshinaga, N., 1972.
564 Imogolite, a hydrated aluminium silicate of tubular structure. Nature Physical Science
565 240, 187–189. https://doi.org/10.1038/physci240187a0

566 Creton, B., Bougeard, D., Smirnov, K.S., Guilment, J., Poncelet, O., 2008. Molecular
567 dynamics study of hydrated imogolite. Phys. Chem. Chem. Phys. 10, 4676–4677.
568 https://doi.org/10.1039/b812223g

D'Angelo, A., Paineau, E., Rouzière, S., Elkaim, É., Goldmann, C., Toquer, D., Rols, S., Launois, P., 2023. The atomic structure of imogolite nanotubes: A 50 years old issue reinvestigated by X-ray scattering experiments and molecular dynamics simulations. Appl Clay Sci 242, 107043. https://doi.org/10.1016/j.clay.2023.107043

Farmer, V.C., Fraser, A.R., 1978. Synthetic imogolite, a tubular hydroxyaluminum silicate, in: Proc. Int. Clay Conf., Oxford. pp. 547–553.

Fernandez-Martinez, A., Michot, L.J., 2016. Physicochemical properties of imogolite, in: Yuan, P., Thill, A., Bergaya, F. (Eds.), Developments in Clay Science. Bergaya, F. , pp. 202–222. https://doi.org/10.1016/B978-0-08-100293-3.00009-1

Gigot, A., Fontana, M., Serrapede, M., Castellino, M., Bianco, S., Armandi, M., Bonelli, B., Pirri, C., Tresso, E., Rivolo, P., 2016. Mixed 1T–2H phase MoS_2/reduced Graphene Oxide as active electrode for enhanced supercapacitive performance. ACS Appl. Mater. Interfaces 8, 32842–32852. https://doi.org/10.1021/acsami.6b11290

Gorgolis, G., Galiotis, C., 2017. Graphene aerogels: a review. 2d Mater 4. https://doi.org/10.1088/2053-1583/aa7883

Han, S., Wu, D., Li, S., Zhang, F., Feng, X., 2014. Porous graphene materials for advanced electrochemical energy storage and conversion devices. Adv. Mater. 26, 849–864. https://doi.org/10.1002/adma.201303115

Iwasaki, M., Yamazaki, K., Banno, K., Shinjoh, H., 2008. Characterization of Fe/ZSM-5 DeNOx catalysts prepared by different methods: relationships between active Fe sites and NH_3-SCR performance. J Catal 260, 205–216. https://doi.org/10.1016/j.jcat.2008.10.009

Kumar, M.S., Schwidder, M., Grünert, W., Bentrup, U., Brückner, A., 2006. Selective reduction of NO with Fe-ZSM-5 catalysts of low Fe content: Part II. Assessing the

592 function of different Fe sites by spectroscopic in situ studies. J. Catal. 239, 173–186.
593 https://doi.org/10.1016/j.jcat.2006.01.024

594 Mackenzie, K.J.D., 1989. Structure and thermal transformations of imogolite studied by ^{29}Si
595 and ^{27}Al high-resolution solid-state Nuclear Magnetic Resonance. Clay Clay Miner. 37,
596 317–324. https://doi.org/10.1346/CCMN.1989.0370404

597 Ma, L., Li, J., Arandiyan, H., Shi, W., Liu, C., Fu, L., 2012. Influence of calcination
598 temperature on Fe/HBEA catalyst for the selective catalytic reduction of NO_x with NH_3,
599 in: Catal. Today. pp. 145–152. https://doi.org/10.1016/j.cattod.2011.10.007

600 Monet, G., Amara, M.S., Rouzière, S., Paineau, E., Chai, Z., Elliott, J.D., Poli, E., Liu, L.M.,
601 Teobaldi, G., Launois, P., 2018. Structural resolution of inorganic nanotubes with
602 complex stoichiometry. Nat Commun 9. https://doi.org/10.1038/s41467-018-04360-z

603 Nasi, R., Sannino, F., Picot, P., Thill, A., Oliviero, O., Esposito, S., Armandi, M., Bonelli, B.,
604 2020. Hybrid organic-inorganic nanotubes effectively adsorb some organic pollutants in
605 aqueous phase. Appl. Clay Sci. 186, 105449. https://doi.org/10.1016/j.clay.2020.105449

606 Picot, P., Gobeaux, F., Coradin, T., Thill, A., 2019. Dual internal functionalization of imogolite
607 nanotubes as evidenced by optical properties of Nile red. Appl. Clay Sci. 178, 1015133.
608 https://doi.org/10.1016/j.clay.2019.105133

609 Shafia, E., Esposito, S., Armandi, M., Bahadori, E., Garrone, E., Bonelli, B., 2016. Reactivity
610 of bare and Fe-doped alumino-silicate nanotubes (imogolite) with H_2O_2 and the azo-dye
611 Acid Orange 7. Catal. Today 277, 89–96. https://doi.org/10.1016/j.cattod.2015.10.011

612 Shafia, E., Esposito, S., Manzoli, M., Chiesa, M., Tiberto, P., Barrera, G., Menard, G., Allia,
613 P., Freyria, F.S., Garrone, E., Bonelli, B., 2015. Al/Fe isomorphic substitution versus
614 Fe_2O_3 clusters formation in Fe-doped aluminosilicate nanotubes (Imogolite). J. Nanopart.
615 Res. 17. https://doi.org/10.1007/s11051-015-3130-2

Tamang, S., Rai, S., Bhujel, R., Bhattacharyya, N.K., Swain, B.P., Biswas, J., 2023. A concise review on GO, rGO and metal oxide/rGO composites: fabrication and their supercapacitor and catalytic applications. J. Alloys. Compd. https://doi.org/10.1016/j.jallcom.2023.169588

Teobaldi, G., Beglitis, N.S., Fisher, A.J., Zerbetto, F., Hofer, W.A., 2008. Hydroxyl vacancies in single-walled aluminosilicate and aluminogermanate nanotubes. J. Phys. Condens. Matter 21, 195301. https://doi.org/10.1088/0953-8984/21/19/195301

Thommes, M., Kaneko, K., Neimark, A. V., Olivier, J.P., Rodriguez-Reinoso, F., Rouquerol, J., Sing, K.S.W., 2015. Physisorption of gases, with special reference to the evaluation of surface area and pore size distribution (IUPAC Technical Report). Pure Appl. Chem. 87, 1051–1069. https://doi.org/10.1515/pac-2014-1117

Van Der Gaast, S.J., Wada, K., Wada, S.-I., Kakuto, Y., 1985. Small-angle X-ray powder diffraction, morphology, and structure of allophane and imogolite. Clay Clay Miner. 33, 237–243.

Wada, K., Yoshinaga, N., Yotsumoto, H., Ibe, K., Aida, S., 1970. High resolution electron micrographs of imogolite. Clay Miner. 8, 487–489.

Wada, S.-I., Eto, A., Wada, K., 1979. Synthetic allophane and imogolite. Journal of Soil Science 30, 347–355. https://doi.org/10.1111/j.1365-2389.1979.tb00991.x

Wang, J., Polleux, J., Lim, J., Dunn, B., 2007. Pseudocapacitive contributions to electrochemical energy storage in TiO_2 (anatase) nanoparticles. J. Phys. Chem. C 111, 14925–14931. https://doi.org/10.1021/jp074464w

Wang, Y., Zhang, L., Hou, H., Xu, W., Duan, G., He, S., Liu, K., Jiang, S., 2021. Recent progress in carbon-based materials for supercapacitor electrodes: a review. J. Mater. Sci. 56, 173–200. https://doi.org/10.1007/s10853-020-05157-6

Wang, Y., Zhang, Q., Shishido, T., Takehira, K., 2002. Characterizations of iron-containing MCM-41 and its catalytic properties in epoxidation of styrene with hydrogen peroxide. J. Catal. 209, 186–196. https://doi.org/10.1006/jcat.2002.3607

Xia, Q., Xu, M., Xia, H., Xie, J., 2016. Nanostructured Iron oxide/hydroxide-based electrode materials for supercapacitors. ChemNanoMat 2, 588–600. https://doi.org/10.1002/cnma.201600110

Yoshinaga, N., Aomine, S., 1962. Imogolite in some ando soils. Soil Sci Plant Nutr 8, 22–29. https://doi.org/10.1080/00380768.1962.10430993

Zanzottera, C., Armandi, M., Esposito, S., Garrone, E., Bonelli, B., 2012a. CO_2 adsorption on aluminosilicate single-walled nanotubes of imogolite type. J. Phys. Chem. C 116, 20417–20425. https://doi.org/10.1021/jp3061637

Zanzottera, C., Vicente, A., Armandi, M., Fernandez, C., Garrone, E., Bonelli, B., 2012b. Thermal collapse of single-walled alumino-silicate nanotubes: transformation mechanisms and morphology of the resulting lamellar phases. J. Phys. Chem. C 116, 23577–23584. https://doi.org/10.1021/jp3090638

Zanzottera, C., Vicente, A., Celasco, E., Fernandez, C., Garrone, E., Bonelli, B., 2012c. Physico-chemical properties of imogolite nanotubes functionalized on both external and internal surfaces. J. Phys. Chem. C 116, 7499–7506. https://doi.org/10.1021/jp301177q